



Aalborg Universitet

AALBORG UNIVERSITY
DENMARK

High-Resolution Structure-from-Motion for Quantitative Measurement of Leading-Edge Roughness

Schou Nielsen, Mikkel; Nikolov, Ivan Adriyanov; Kruse, Emil Krog; Garnæs, Jørgen ; Madsen, Claus B.

Published in:
Energies

DOI (link to publication from Publisher):
[10.3390/en13153916](https://doi.org/10.3390/en13153916)

Publication date:
2020

Document Version
Early version, also known as pre-print

[Link to publication from Aalborg University](#)

Citation for published version (APA):

Schou Nielsen, M., Nikolov, I. A., Kruse, E. K., Garnæs, J., & Madsen, C. B. (2020). High-Resolution Structure-from-Motion for Quantitative Measurement of Leading-Edge Roughness. *Energies*, 13(15), Article 3916. <https://doi.org/10.3390/en13153916>

General rights

Copyright and moral rights for the publications made accessible in the public portal are retained by the authors and/or other copyright owners and it is a condition of accessing publications that users recognise and abide by the legal requirements associated with these rights.

- Users may download and print one copy of any publication from the public portal for the purpose of private study or research.
- You may not further distribute the material or use it for any profit-making activity or commercial gain
- You may freely distribute the URL identifying the publication in the public portal -

Take down policy

If you believe that this document breaches copyright please contact us at vbn@aub.aau.dk providing details, and we will remove access to the work immediately and investigate your claim.

Article

High-resolution Structure-from-Motion for quantitative measurement of leading edge roughness

Mikkel Schou Nielsen ¹, Ivan Nikolov ², Emil Krog Kruse ³, Jørgen Garnæs ¹ and Claus Madsen ²

¹ Danish Fundamental Metrology: Kogle Allé 5, DK-2970, Hørsholm

² Aalborg University: Rendsburggade 14, DK-9000, Aalborg

³ Power Curve ApS: Kastetvej 2, DK-9000, Aalborg

* Correspondence: Mikkel Schou Nielsen msn@dfm.dk

Version September 1, 2020 submitted to Energies

Abstract: Over time, erosion of the leading edge of wind turbine blades increases the leading edge roughness (LER). This may reduce the aerodynamic performance of the blade and hence the annual energy production of the wind turbine. As early detection is key for cost-effective maintenance, inspection methods are needed to quantify the LER of the blade. The aim of this proof-of-principle study is to determine whether high-resolution Structure-from-Motion (SfM) has the sufficient resolution and accuracy for quantitative inspection of LER. SfM provides 3D reconstruction of an object geometry using overlapping images of the object acquired with a RGB camera. Using information of the camera positions and orientations, absolute scale of the reconstruction can be achieved. Combined with a UAV platform, SfM has the potential for remote blade inspections with a reduced down-time. The tip of a decommissioned blade with an artificially enhanced erosion was used for the measurements. For validation, replica moulding was used to transfer areas-of-interest to the lab for reference measurements using confocal microscopy. The SfM reconstruction resulted in a spatial resolution of 1 mm as well as a sub-mm accuracy in both the RMS surface roughness and the size of topographic features. In conclusion, high-resolution SfM demonstrated a successful quantitative reconstruction of LER.

Keywords: Structure from Motion; Surface Analysis; Leading Edge Roughness; Blade inspection; Quantitative 3D reconstruction; Photogrammetry

1. Introduction

Erosion of wind turbine blades poses a challenge for wind energy operation and maintenance [1]. Erosion of the leading edge (LE) increases the surface roughness and reduces the aerodynamic performance of the blade [1,2]. As the shape of wind turbine blades is specifically designed to achieve maximum energy efficiency [3], this increased leading edge roughness (LER) may lead to a reduced annual energy production of the wind turbine. Through CFD modelling, several studies have found that even a small degree of LE erosion can lead to 2%-5% loss in annual energy production [4–6]. Severely eroded blades with high levels of LER can experience losses from 8% and up to 25% [4,7,8]. As LE erosion over time can develop from small pinholes to large areas of coating delamination [4,9], early detection of the severity of the erosion is important. At later erosion stages, extensive blade repair may be necessary causing expensive turbine down-time. Thus for early erosion detection, inspection methods for measuring the surface topography of the blade are needed to quantify the LER.

Visual inspection have long been applied for condition-monitoring of wind turbine blades [10]. In recent years, unmanned aerial vehicles (UAV) have received increased interest for remote inspection of wind turbines [11–16] with a lower downtime compared to manual rope-access inspection. From

2D images captured by the UAV, deep learning methods [13,15] can be used for detecting damages and erosion on the blades. However, while the 2D information can reveal the presence and location, *quantification* of the blade surface roughness requires high-resolution 3D data.

Structure-from-Motion (SfM) is a camera-based method that provides a 3D reconstruction of an object geometry with a simple, fast and low-cost acquisition [17–19]. Aided by a rapid development of both open source [20,21] and commercial software solutions [22–24], SfM has found industrial interest in e.g. construction site monitoring [25–27] and infrastructure inspection [28–32]. A lot of research has also been done in the performance of SfM, for different use cases [33,34]. As input for the SfM reconstruction, overlapping images of the object from different positions and orientations are acquired using a RGB camera. Feature points are extracted and matched between the 2D input images using local feature descriptors such as SIFT [35] or ORB [36]. From the feature points and intrinsic camera parameters, a sparse 3D point cloud as well as the camera positions and orientations are computed. Using information from reprojected camera views, further points can be added to create a dense point cloud, which can be further meshed [37,38].

The accuracy of a SfM reconstruction is influenced by a number of factors. Since SfM depends on triangulation of feature points, the accuracy is affected by the angular coverage of the acquired images [19,39] and scales with the capturing distance from camera to object [38,40,41]. Furthermore, a sufficient texture level is required for enough distinct features on the object surface to be tracked from image to image [19,42]. Low texture regions may result in empty regions of the point cloud [43]. To evaluate the accuracy, the SfM reconstruction is typically compared to another optical technique such as a LiDAR or laser scanner. This can be done either by direct point-to-point comparison with the SfM point cloud [19,44,45] or raster-to-raster comparison of digital elevation models (DEM) [46,47]. Either way, the comparison is influenced by the measurement uncertainty of the reference points [47]. Common metrics for reporting the accuracy are the standard deviation (SD) [17,33,44] and root mean square deviation (RMSD) [41,43,46].

Within wind energy, SfM has previously been investigated for 3D reconstruction of blade geometries [11,16]. However, these studies did not have a sufficient resolution to reconstruct the surface topography directly and rather used the color texture to identify damages. With high-resolution SfM, a point-sampling distance below 0.1 mm/pixel can be achieved which allows for reconstruction of the surface roughness [48,49].

In this proof-of-principle study, we investigate the potential of high-resolution SfM in quantitative inspection of wind turbine blades. We envisage a scenario where an UAV carrying a high-end RGB camera is capturing images of the LE of blades. Using these images, a SfM reconstruction of (parts of) the LE is performed from which quantitative measures of the LER can be extracted. The study seeks to answer two main questions. Firstly, to demonstrate whether a sufficient resolution can be achieved to reconstruct the LER of a blade. Secondly, what **is** the performance of high-resolution SfM in providing quantitative measures of the surface topography of the LER. A mock-up of an eroded blade was fabricated by artificially enhancing the LER of the tip of a decommissioned blade. The SfM capturing was done using a handheld camera and in an outdoor environment to mimic realistic inspection conditions. In the high-resolution acquisition, the images were acquired from a distance of roughly 2 meters using a 300 mm lens. We believe these conditions to be representative of what the envisaged UAV inspection scenario might operate with.

For evaluating the accuracy of the SfM reconstruction, selected areas on the blade surface were extracted from the point cloud and converted to a DEM. Replicas of the same areas on the blade surface were made using replication moulding and transferred to the lab. Replication moulding is a demonstrated method for transferring hard-to-access surface topographies to a substrate suitable for microscopy measurements [50]. In the replication of surface roughness, accuracies at the sub-micrometer level have been demonstrated using elastomer replica materials [51–56]. Using confocal microscopy (CM) measurements of the replicas, a DEM was created for direct raster-to-raster comparison to the SfM reconstruction. The resolution of the SfM reconstruction was evaluated

83 using Fourier analysis and RMSD calculation. For validation of the resolution analysis, a model was
84 constructed by reducing the resolution of the reference DEM and adding noise. This model DEM
85 was then compared to the SfM DEM. Finally, the quantitative performance in measuring LER was
86 evaluated using surface roughness parameters and topographic feature sizes.

87 2. Methods and Materials

88 2.1. Blade Mock-up

89 A decommissioned wind turbine blade was available for the experimental setup. The blade had
90 been used in a modern 2 MW pitch-regulated wind turbine. Span-wise, the outer two meters of the
91 blade that already had some erosion was used. To better resemble the examples of severe LE erosion
92 experienced from field inspections [4,8,9], the erosion was artificially increased by sandblasting the
93 LE. At this level of erosion, large areas of laminate are exposed along the LE with depths of 1-3 mm.
94 Severe erosion was chosen for this study for two main reasons. Firstly, depths of these magnitude are
95 at the order where the aerodynamic performance is significantly impacted. A study by Bak *et al.* [57]
96 found that the critical height of roughness for lowering the maximum lift of wind turbine blades was
97 above 1 mm. Secondly, a large surface roughness represents a good pass/fail test of the feasibility of
98 high-resolution SfM. If the resolution was not sufficient for resolving large erosion structures, it would
99 not function for less eroded surfaces either.

100 For inspection of a wind turbine in operation, we envision that the turbine is stopped with the
101 inspected blade in a vertical position. To simulate this, the blade was mounted vertically in a gantry,
102 which was welded together for the purpose of this work. To include the effect of oscillations, chain
103 links were used to fix the blade mock-up to the gantry, which let the blade segment move freely in the
104 wind. The height of the gantry was 5 meters, resulting in a distance of 5 meters from the very tip of the
105 blade to the ground. The blade setup on the gantry, together with the scissor lift used to capture all the
106 data for this paper can be seen in Figure 1.



Figure 1. The wind turbine blade segment positioned on the built gantry, together with the scissor lift used for capturing image and replica data.

107 2.2. SfM Capturing Conditions

108 The image capturing process of the proof-of-principle study was done in an outdoor environment
109 to ensure realistic capturing conditions. A commercial DSLR camera (Canon 5Ds) with a variable
110 zoom lens (Canon 70-300 f/4-5.6L IS USM) was used with the focal length fixed at 300 mm. Camera

111 parameters and settings are summarized in Table 1. As the capturing was done outdoors, a number of
 112 prerequisites need to be taken into account:

- 113 • The natural illumination can change between images.
- 114 • The sides of the blade mock-up may not be evenly illuminated.
- 115 • Wind can cause oscillations of the blade mock-up, which can change its position and orientation
 116 compared to previous images.

117 Since the accuracy of the SfM reconstruction depends on the stability of light conditions, camera
 118 settings should be robust to environmental changes in light direction and intensity. **In addition, the
 119 settings should take into account the possible motion of the blade.** The chosen ISO, shutter, and
 120 aperture settings are shown in Table 1. They represent what we believe to be reasonable compromises
 121 between exposure for outdoor conditions, becoming less sensitive to motion blur (shutter) and not
 122 having to worry too much about too shallow depth-of-field (aperture).

Table 1. Camera parameters and settings for the outdoor capturing setup.

Camera Parameters	Values
ISO	800
Shutter Speed [sec]	1/200
Aperture	f/16
Focal length [mm]	300
Image size [pixels]	8688x5792
Sensor pixel size [μm]	4.14
Capturing setup	
Distance to blade [m]	2
Angular spacing [$^\circ$]	10
Capturing bands	3
No of images	57
GSD [$\mu\text{m}/\text{pixel}$]	27

123 For the initial proof-of-principle study, a manual and hand-held image capturing was performed.
 124 A part of the wind turbine blade was chosen that contained a variation in surface topography across
 125 the leading edge - from very rough damaged areas to smoother clean areas. The part of the blade
 126 chosen for 3D reconstruction is shown in Figure 2.

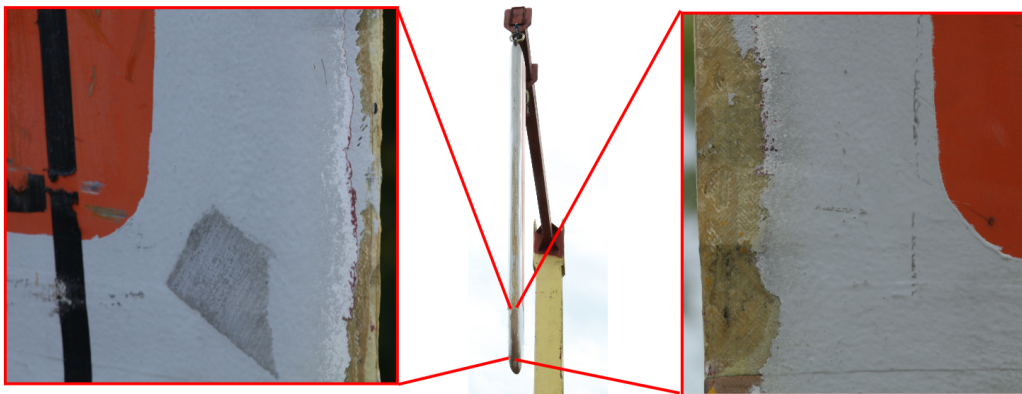


Figure 2. Testing blade together with the region chosen for reconstruction. The zoomed-in parts are of the two sides of the blade

127 A semi-circular 180-degree capturing pattern is used for the image capturing. This capturing
 128 method was shown by [34] and [58] to produce high accuracy reconstructions, while also minimizing

129 the number of required images. Three horizontal semi-circular bands each with 19 images were
 130 acquired giving a total of 57 images. To ensure enough vertical separation between the horizontal
 131 bands, the first band was taken from the ground level looking toward the suspended blade. To capture
 132 the other two bands a moving scissor lift was used. The captured positions can be seen in Figure 3b.
 133 This way the blade surface could be captured from different positions and angles both in horizontal
 134 and vertical direction, ensuring maximum cover. The semi-circles were centered around the wind
 135 turbine blade with a distance of 2 meters from camera to blade. The capturing settings are summarized
 136 in Table 1.

137 For a fixed focal length, the capturing distance determines the ground sampling distance (GSD),
 138 i.e. the spatial size on the object that each pixel in a captured image covers. Using a pinhole camera
 139 model, the GSD can be calculated as the camera sensor pixel size p multiplied by the ratio of the
 140 distance between camera and surface D over the focal length f as shown in equation 1.

$$GSD = \frac{D}{f} p \quad (1)$$

141 With the used settings in the study, the GSD was $27 \mu\text{m} / \text{pixel}$ which corresponds to approximately
 142 36 pixels/mm on the blade surface.

143 2.3. SfM Reconstruction

144 For SfM reconstruction, the commercial stand-alone software package Agisoft Metashape by [22]
 145 was used. It was selected as it has previously demonstrated a high accuracy compared to other state of
 146 the art solutions, while being robust against sub-optimal capturing conditions [34]. The pipeline from
 147 input images, 3D reconstruction and extraction of depth map patches is visualized in Figure 3. An
 148 overview of the process is given below.

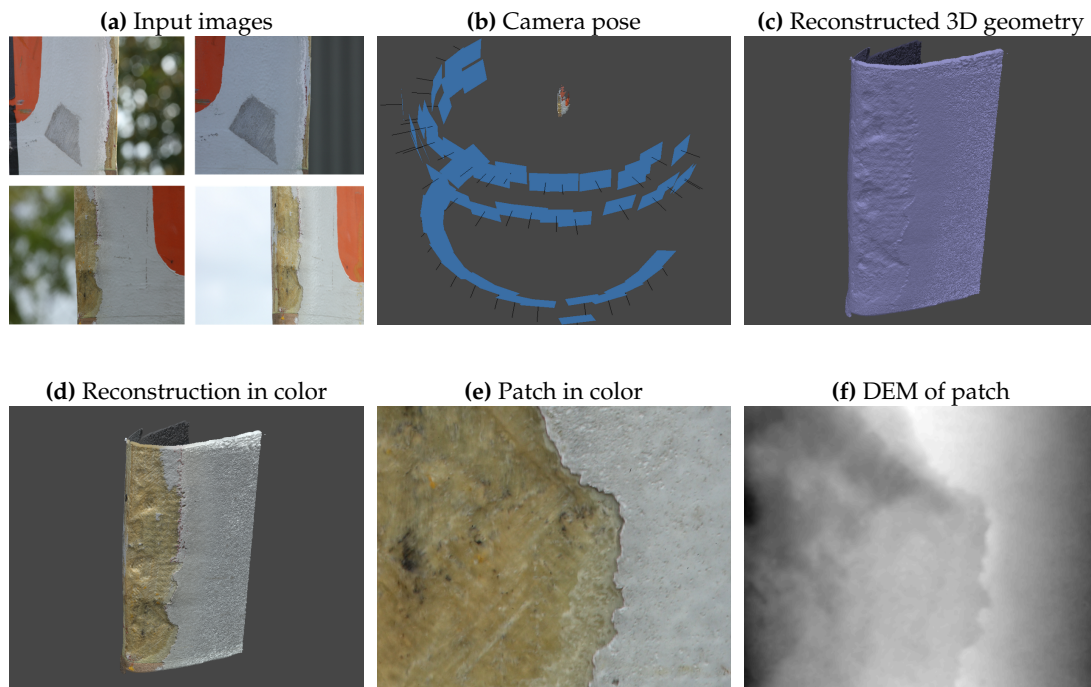


Figure 3. Pipeline for 3D reconstruction using SfM. 3a) Initially, images were acquired at every 10 degrees of a half circle around the wind turbine blade at three different heights and tilt angles. 3b) The camera pose of the images and points on the object surface were then calculated. The reconstructed surface geometry without 3c and with color 3d. Extracted patch from the reconstruction shown as 3e (color) texture and 3f resulting DEM.

149 The captured images 3a were imported to Metashape and a triangulation, feature extraction and
150 matching step were performed to find the camera positions and key feature points from the input
151 images 3b. From these positions and feature points, a sparse point cloud was formed. Next in the
152 reconstruction process a dense point cloud was created and meshed into a triangle mesh 3c. Finally a
153 (color) texture is build from the visual data from the input images 3d.

154 To establish an absolute scale in the SfM reconstruction, the known camera positions and distance
155 from camera to blade surface were utilized. The method presented in [59] was followed. The scale was
156 calculated using a least squares transformation estimation between the reconstructed camera positions
157 and the manually measured positions in the real world.

158 For evaluating the SfM reconstruction, three areas R1, R2 and R3 were selected for comparison to
159 reference microscopy measurements. The areas were chosen to include distinctive surface topography
160 features and cover the boundary between intact coating and damaged surface. For each area, a
161 digital elevation model (DEM) was created from the reconstruction using the following pipeline. First,
162 for further processing and analysis of the mesh the reconstruction was imported to the software
163 CloudCompare [60]. For each area, a patch of roughly 35 mm x 35 mm was created from the main
164 reconstructed point cloud. The patches were oriented with the Z axis perpendicular to the mesh surface,
165 and were rasterized into a DEM of the surface topography 3f. This was done by an interpolation of the
166 point-cloud points to a map with equidistant point spacing and using the average *z-values* of each grid
167 space. The resulting pixel size was chosen to be 13,3 μm to match the reference microscopy images.

168 2.4. Replica Moulding

169 Replication was performed for each of the R1, R2 and R3 areas described in section 2.3. As a
170 replication material with a fast curing time and resolution down to 0.1 μm , Repliset T3 by Struers [61]
171 was selected. In previous studies, the replication of surface textures using Repliset has achieved a
172 sub-micrometer accuracy [55,62]. The RepliSet T3 is a black two-part silicone rubber which consists of
173 a polymer and curing agent. For replication, the two parts were pushed out of the cartridge, mixed in
174 a static-mixing nozzle and applied onto the blade surface 4a. Immediately after application, backing
175 paper was placed on top of the mixture and attached by applying a small force as shown in Figure 4b.
176 The mixture set for 15 minutes and then the replica was removed from the blade surface by hand.



Figure 4. Replication of an area on the blade mock-up. Figure 4a illustrates the application of the combined polymer and curing agent from a static-mixing nozzle. Figure 4b shows the backing paper being attached by applying a gentle force to the replication material.

177 2.5. Confocal microscopy

178 Confocal microscopy (CM) was used to produce reference DEMs of the R1, R2 and R3 areas. The
179 three replica of the blade surface were measured using a calibrated PLU NEOX confocal microscope by
180 Sensofar [63]. For each replica, an extended area of approx. 35 mm x 35 mm was measured by stitching

181 around 400 individual images. A x5 magnification objective with an NA of 0.15 was used. For each
 182 image, a 4x4 binning was used resulting in a final pixel size of 13.3 μm . To ensure a superior resolution
 183 for the CM measurement, the pixel size was kept smaller than the GSD of the SfM reconstruction. The
 184 vertical step size (*z-axis*) used was 12 μm . The 3D surface reconstruction, stitching and creation of a
 185 DEM were performed using the proprietary SensoSCAN software.

186 The sensitivity of the CM microscope in the vertical direction (*z-axis*) was calibrated using a set of
 187 step height transfer standards. Traceability was ensured through calibration of the standards by e.g.
 188 an AFM equipped with laser interferometer. The amplification coefficient of the *z-axis* had a relative
 189 uncertainty **lower** than 3%.

190 2.6. Image processing and data analysis

191 The main software programs used for the surface topography analysis were the Scanning Probe
 192 Image Processor (SPIP) [64] version 6.6.3 as well as custom scripts in MATLAB version 2019b. SPIP is
 193 an image processing program with special tools for accurate characterization of image structures.

194 Initially using SPIP, each SfM and reference DEM were levelled by subtracting a least-squares
 195 parabola fit from the overall shape. This way the long wavelength curvature of the surface was
 196 removed, while the short wavelength surface roughness could be preserved. Then for each area, the
 197 SfM DEMs were co-registered using a Fourier correlation approach in MATLAB.

198 From the co-registered DEMs, geometrical quantities were extracted from both SfM and
 199 microscopy reference. The chosen quantities are the depth and height of topographic features.

200 2.6.1. SfM reconstruction quality

201 To evaluate the quality of the SfM reconstruction, two parameters were chosen; The instrument
 202 transfer function at 50% value (ITF50) and the maximum value of the cross-correlation function
 203 (CCF_{max}).

204 The ITF50 value is a measure of the spatial sharpness, which is analogous to the MTF50 value of
 205 the modulation transfer function. ITF50 is found as the spatial wavelength at which the instrument
 206 response is half the value of the reference. The definition of ITF is shown in (2) [65]. For the calculation,
 207 a region on the surface containing a height is selected. For each line across the height step, the ratio of
 208 the 1D Fourier transforms of the instrument function and reference is calculated. The ITF is found as
 209 the mean of all lines in the region.

$$ITF(f) = \left\langle \frac{\left| \int_{-\infty}^{\infty} z(x, y) e^{-i2\pi f x} dx \right|}{\left| \int_{-\infty}^{\infty} z_{ref}(x, y) e^{-i2\pi f x} dx \right|} \right\rangle_y \quad (2)$$

CCF_{max} has a value between 0 and 1 and describes the spatial similarity of a set of co-registered
 measurement and reference topographies. If the measurement is very close to the reference, the value
 of CCF_{max} will be close to 1. CCF_{max} is found as the maximum of the normalized 2D cross-correlation
 function [66].

$$f_{\text{CCF}}(t_x, t_y) = \frac{\iint_A z(x, y) z_{ref}(x - t_x, y - t_y) dx dy}{\sqrt{\iint_A z^2(x, y) dx dy \iint_A z_{ref}^2(x, y) dx dy}} \quad (3)$$

210 2.6.2. Surface Roughness

211 Prior to performing the surface roughness analysis, an S-filter of 25 μm and an L-filter of 10 mm
 212 were applied to the DEM in accordance with [67]. A plane was chosen as reference surface using
 213 a least-squares linear fit to the height values of the DEM. The following areal surface roughness
 214 parameters as described in [68] were calculated: S_q , S_{dq} and S_{al} . These parameters were chosen as they

215 describe different and complementary features of the surface topography as explained below. The
 216 analysis was performed using the "Roughness Analysis" tool of the SPIP application software.

- 217 • S_q is the root mean square height of the **z-values** with respect to the reference surface. S_q describes
 218 the overall height variation of the DEM.
- 219 • S_{dq} is the root mean square of the surface gradient. As S_{dq} depends on variations in the local
 220 slope, it is sensitive to the short wavelength components of the surface topography.
- 221 • S_{al} is the auto-correlation length, and is a measure of the spatial distance at which the surface
 222 texture becomes statistically different. S_{al} is calculated as the minimum distance in frequency
 223 space at which the auto-correlation function decays to 0.2 in value. Therefore, S_{al} contains
 224 information on the long wavelength components of the surface topography.

225 3. Results

226 The performance of the SfM reconstruction is illustrated in Figure 5. In 5a and 5b, the SfM and
 227 reference DEM of replication area R1 are shown. Both have been processed as described in section
 228 2.6. The blue box indicates the subregion used for the ITF analysis. As seen in panel 5a, the SfM DEM
 229 captures the main topographic features although the resolution is less than for the reference in 5b.
 230 While short wavelength topography variations are missing, holes, edges and the larger glass-fiber
 231 structures are visible in the SfM DEM.

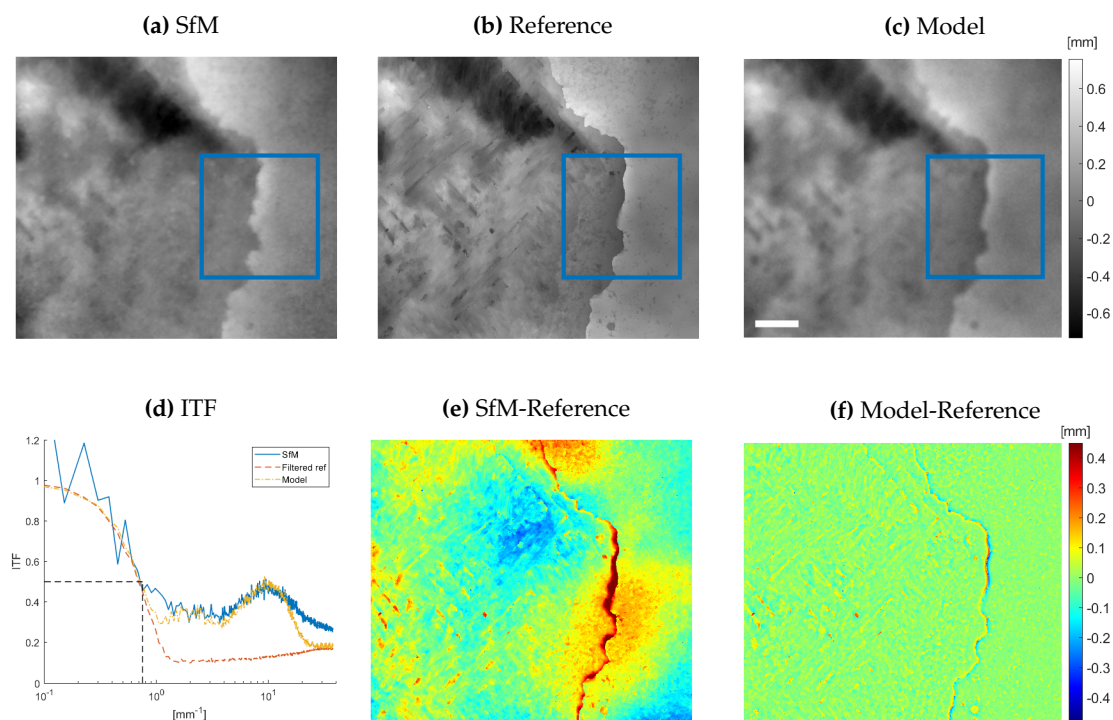


Figure 5. 5a Reference, 5b SfM and 5c model DEM of replication area R1. The blue box indicates the area used for the calculation of ITF50. The scalebar is 5 mm. 5d ITF for SfM and two model curves based on filtering the reference DEM with and without noise added. 5e-5f Residual of SfM and model DEM with respect to reference DEM.

232 The ITF function was calculated from the SfM and Reference DEM of area R1 as described in
 233 section 2.6.1. The ITF was not calculated for R2 and R3 as no height step was present in these areas. In
 234 5d, the ITF function for SfM is shown (blue solid line) with the 50% value indicated in dashed black
 235 lines. As stated in Table 2, the ITF50 spatial wavelength was 1.3 mm.

236 In order to validate the shape of the SfM ITF, a model was developed based on the reference DEM.
 237 First, the reduced resolution of the SfM reconstruction was approximated by applying a Gaussian

low-pass filter to the reference DEM. A filter with a FWHM of 0.65 mm was used to give the model DEM the same ITF50 value as the SfM. As seen in Figure 5d, the ITF of the filtered reference (dashed red line) matches the long wavelength values of the SfM ITF. However, at higher frequencies the filtered reference has lower values than the SfM. In a second step, structured noise centered at 0.5 mm and 0.1 mm wavelengths was added (dash-dotted yellow line). The two noise components was constructed through Gaussian low-pass filtering of Gaussian noise with an amplitude selected to match the SfM ITF. In 5c, the model DEM using Gaussian filter and noise added is shown for area R1. Similarly, a model DEM was created for both area R2 and R3 using the same Gaussian FWHM and noise settings.

In Table 2, CCF_{max} and RMSD values for both SfM and model DEM are shown for all replication areas. The CCF_{max} values for the model were close to 1 for all areas. For SfM, the values were >0.9 for both R2 and R3 indicating a very close horizontal spatial resemblance. A slightly smaller value was found for R1. Overall, the CCF_{max} values indicate that an accurate scaling of SfM was obtained. As seen in the table, the RMSD values for SfM are between 0.1-0.2 mm, which is several times larger than the model values between 0.03-0.04 mm. This discrepancy is illustrated in the residuals shown in Figure 5e and 5f. While large differences are observed near sharp edges for both model and SfM DEM, the SfM residuals also contain a waviness that accounts for the larger RMSD value. The waviness has a wavelength in the order of 10 mm which shows up as large variations in the long wavelength part of the ITF in Figure 5d.

Table 2. Quantitative values for evaluating the SfM reconstruction. CCF_{max} and RMSD are included for all three areas R1 to R3 while ITF50 was only calculated for R1.

Replication area	R1	R2	R3
ITF50 [mm]	1.3		
CCF_{max} , SfM	0.86	0.95	0.93
CCF_{max} , Model	0.98	0.99	0.995
RMSD, SfM [mm]	0.099	0.12	0.21
RMSD, Model [mm]	0.038	0.036	0.031

To evaluate the surface roughness of the SfM reconstruction, two regions within each of the R1, R2 and R3 areas were selected as shown with blue solid lines in Figure 6a to 6c. Of the six regions named S1 to S6, an extensive erosion of S1 and S3 resulted in a topography dominated by glass-fiber structures while S2, S4, S5 and S6 still had an intact surface coating.

The roughness parameters S_q , S_{dq} and S_{al} were calculated for each of the S1 to S6 regions as described in section 2.6.2. The roughness values for both SfM and reference are shown in Table 3 and illustrated in scatter plots in Figure 6g to 6i. Overall, both SfM and reference values show a larger roughness for the eroded S1 and S3 regions than the regions with intact coating. However, when comparing the three roughness parameters on the scatter plots, some differences are clear. While the SfM values for S_q and S_{al} vary within around 10%-20% of the reference values, the SfM values for S_{dq} are systematically lower than the reference by around 50%. The absolute RMSD deviations for S1 to S6 were 9 μm for S_q , 0.5 for S_{dq} and 0.2 mm for S_{al} .

Three distinctive topographic features were selected in the R1 and R2 areas; Two depressions D1 and D2 (red dashed lines) and a height step H1 (yellow dotted lines) as shown in Figure 6a and 6b. For all features, the depth and height measurements for the SfM DEM are close to the reference as shown in Table 3. The relative deviations between SfM and reference are less than 16%, and the absolute deviations were less than 0.2 mm with an RMSD of 0.1 mm.

4. Discussion

The reconstructed SfM displayed a high sharpness and resolution. From the ITF50 value, we have that features down to 1.3 mm appear sharp. Conversely, the Gaussian FWHM of 0.65 mm from the model DEM gives a measure of the spatial resolution, i.e. the smallest distinguishable features. The

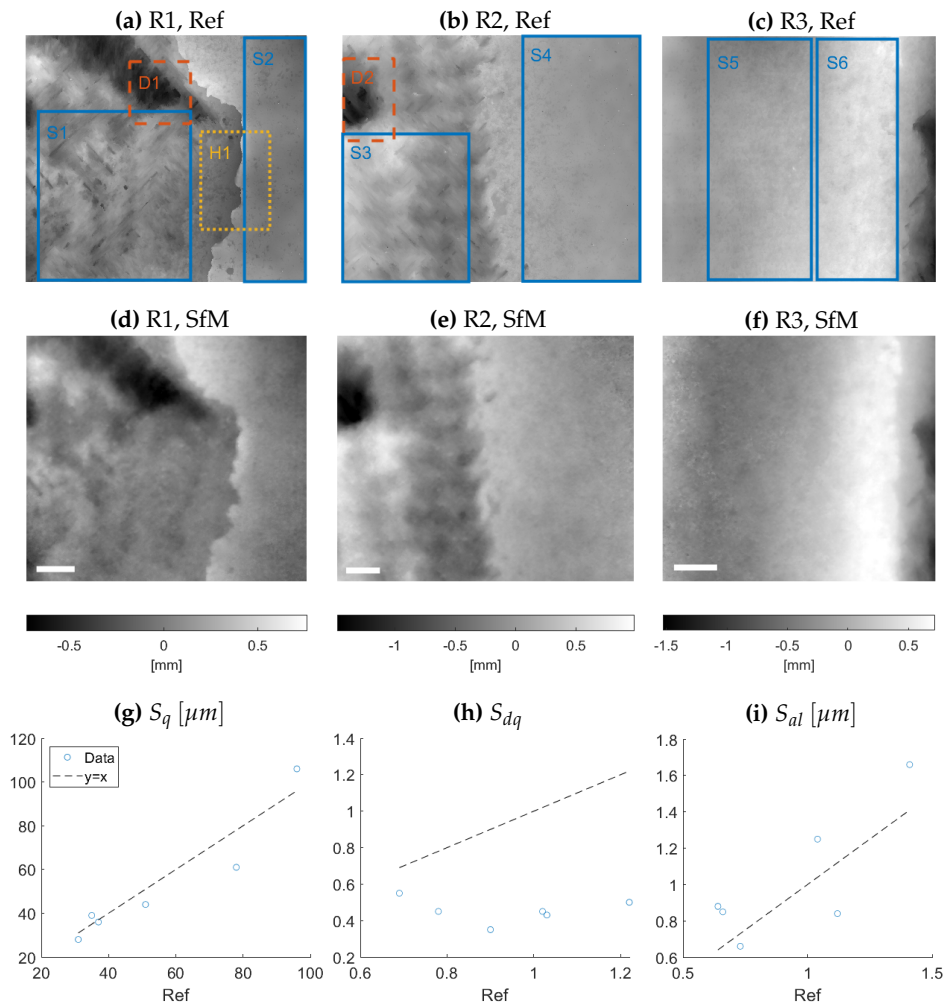


Figure 6. 6a-6c Reference and 6d-6f SfM DEMs of area R1, R2 and R3, respectively, with prior image processing as described in section 2.6. Surface roughness regions S1 to S6 are indicated with solid blue lines. Depressions D1, D2 and ridge H1 are indicated with dashed red and dotted yellow lines, respectively. The scalebar is 5 mm. 6g-6i Scatter plots of SfM and reference values for S_q , S_{dq} and S_{al} , respectively. The dotted line indicates where SfM values are equal to reference values.

278 resolution of around 1 mm is one to two orders of magnitude lower than the GSD of $27 \mu\text{m}$, which is in
 279 line with previous high-resolution SfM studies [48,49].

280 The high value of CCF_{max} for the R2 and R3 areas shows a good spatial resemblance between
 281 SfM and reference measurements. The slightly lower value for R1 could either indicate an insufficient
 282 resolution or an imperfect co-registration. Since the CCF_{max} values for the model DEM were close to 1,
 283 the resolution seems sufficient to preserve the topographic features. The accuracy in co-registering
 284 the DEMs could be limited by the replication moulding. While the replica ensures a high replication
 285 accuracy of the surface roughness, the overall shape is not preserved when demoulding the replica.
 286 Although a levelling was applied, a waviness was still observed in the residual of the SfM DEM with
 287 respect to the reference as seen in Figure 5e. Nonetheless, as the waviness had a wavelength of 10 mm
 288 it did not impact the ITF50 value of 1.3 mm.

289 Furthermore, as indicated by the model DEM, a rather high noise level was present in the SfM
 290 DEM. Some of this may originate from the point cloud densification or the interpolation when creating
 291 the DEM. Varying light intensity may also affect the reconstruction as reported by [11]. Further studies
 292 are needed to determine the potential for reducing the noise level.

Table 3. Quantitative values for surface roughness and topography features. The roughness parameters S_q , S_{dq} and S_{al} for regions S1 to S6 were calculated using an S-filter of $25 \mu\text{m}$ and an L-filter of 10mm . The depth for depression areas D1 and D2 and height for ridge area H1.

Replication area	R1		R2		R3	
	S1	S2	S3	S4	S5	S6
S_q , Ref [μm]	78	31	96	35	37	51
S_q , SfM [μm]	61	28	106	39	36	44
S_{dq} , Ref	1.03	0.78	1.02	1.22	0.69	0.90
S_{dq} , SfM	0.43	0.45	0.45	0.50	0.55	0.35
S_{al} , Ref [mm]	1.04	1.12	1.41	0.66	0.73	0.64
S_{al} , SfM [mm]	1.25	0.84	1.66	0.85	0.66	0.88
	D1	H1	D2			
Δz , Ref [mm]	0.57	0.34	1.51			
Δz , SfM [mm]	0.66	0.30	1.68			

293 The surface roughness analysis show relatively good results for SfM measurement of both S_q and
 294 S_{al} parameters. The resolution of the SfM reconstruction was sufficient as both S_q and S_{al} are most
 295 sensitive to the low spatial frequencies, i.e. structures larger than 1mm . Similarly, the topographic
 296 features D1, H1 and D2 had large spatial widths which ensured good results for the measured depths
 297 and heights. In contrast, a poor result was seen for the S_{dq} parameter which is sensitive to high spatial
 298 frequencies, i.e. structures smaller than 1mm .

299 The potential for using the S_q parameter in quantitative characterization of LER is illustrated in
 300 Figure 7. First, the SfM reconstruction was unfolded to a flat shape and extracted as a DEM using
 301 CloudCompare. A region centered on the LE was selected as indicated with a box in Figure 7b. For
 302 each $10 \text{mm} \times 10 \text{mm}$ square in the region, the S_q parameter was calculated and visualized in red in
 303 Figure 7c. The strength of the red color indicates the S_q value in each square with a lower bound of $20 \mu\text{m}$
 304 (μm (no color) and upper bound of $100 \mu\text{m}$ (color saturated). As seen, the S_q values are low for areas
 305 with the coating still intact, and high along the eroded leading edge. This indicates the potential for
 306 high resolution SfM for quantitative inspection of LER.

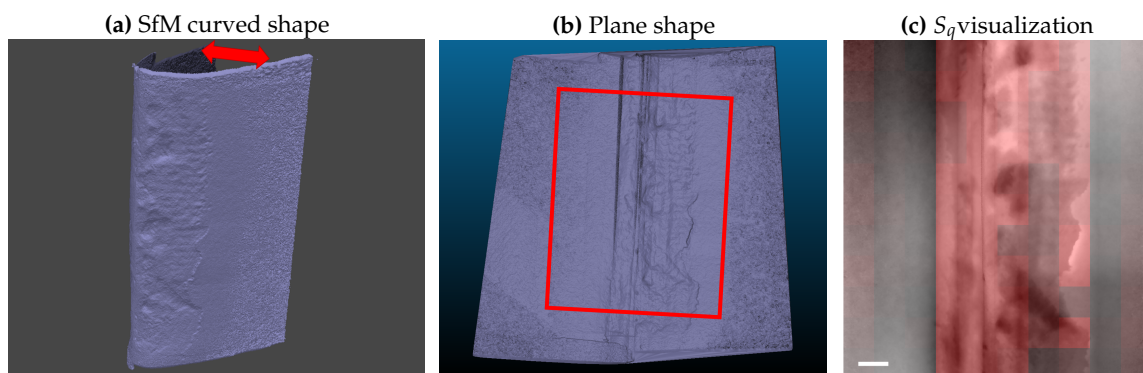


Figure 7. Visualization of LER. The curved blade geometry seen in 7a was unfolded to a flat shape shown in 7b from which a region centered on the LE was selected as indicated by the box. For each $10 \text{mm} \times 10 \text{mm}$ square in the region, the S_q parameter was calculated. In 7c, the strength of the red color indicates the S_q value in each square. The scalebar is 10mm .

307 For quantitative inspection of the blade erosion, the resolution of the SfM reconstruction needs to
 308 match the size of erosion structures, i.e. pits, gauges and delamination. From inspection reports of LE
 309 erosion structures, Sareen *et al.* [4] considered pits and gouges with widths down to 0.5mm and depths
 310 from 0.5mm to 3.8mm . In the study by Gaudern [9], widths down to 2mm and depths from 0.1mm
 311 to 1mm were investigated. In both studies, the delamination covered tens of millimeters in width
 312 and $1\text{--}3 \text{mm}$ in depth. The lower end of these feature sizes correspond very closely to the obtained

313 resolution of 1 mm. Conversely, as the results of the SfM measurements of topographic features D1, H1
 314 and D2 showed, depths from 0.3 mm - 1.5 mm could be successfully measured using high-resolution
 315 SfM.

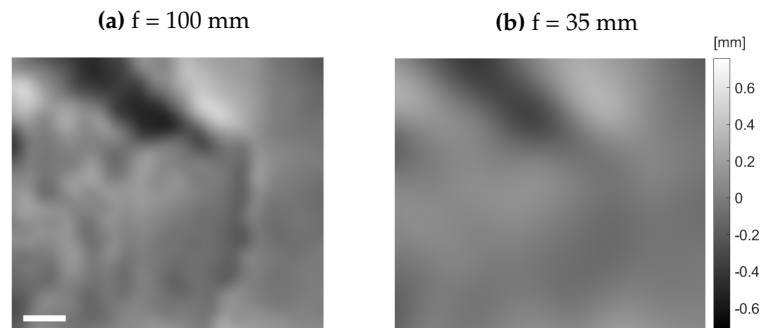


Figure 8. Model DEM of a SfM acquisition of area R1 with 8a 100 mm and 8b 35 mm focal length. The model DEMs were created by Gaussian low-pass filtering of the R1 reference DEM of Figure 5b with FWHM of 1.9 mm and 5.5 mm, respectively. The scalebar is 5 mm.

316 Had the SfM resolution been lower by e.g. using a shorter focal length, the surface roughness
 317 and smaller topographic features would not have been visible. This is illustrated in Figure 8 by a
 318 model DEM of a SfM acquisition of area R1 with a 2 m capturing distance using a 100 mm (8a) or 35
 319 mm (8b) focal length. **These settings correspond to a GSD of 0.08 mm and 0.24 mm, respectively.** The
 320 model DEMs were created from the R1 reference DEM of Figure 5b by applying a Gaussian low-pass
 321 filter with a FWHM of 1.9 mm and 5.5 mm, respectively. As seen, already for the 100 mm focal length,
 322 the glass fiber structures are becoming blurred. For the model of a 35 mm focal length, even the
 323 topographic features appear blurred.

324 **In previous studies which applied SfM to reconstruct blade surface, the low resolution would**
 325 **have made a quantification of LER infeasible. In comparison, the settings used by Wang and Zhang**
 326 **[11], Zhang *et al.* [16] resulted in a GSD of around 0.3 mm which corresponds to the model in Figure**
 327 **8b. Rather than quantifying the surface topography, they relied on the texture of the reconstruction**
 328 **to locate damages on the blade surface. An advantage of using a lower resolution is that a larger**
 329 **surface area of the turbine blade can be covered in a single reconstruction. Applying high-resolution**
 330 **SfM to reconstruct the full length of a blade would require a very long inspection time and result in a**
 331 **challenging amount of data.**

332 **For full blade inspection, 2D images with even lower resolution can be applied which require fewer**
 333 **image acquisitions and a lower acquisition time. However, in this approach the absolute geometry**
 334 **is not obtained, and the LER is not quantified. Instead other methods would be needed to indicate**
 335 **the presence and location of LER such as the deep learning approach used by Shihavuddin *et al.* [13].**
 336 **In many ways, the proposed high-resolution SfM is complementary to this deep learning approach.**
 337 **By combining both, an initial inspection using low-resolution 2D images would indicate the location**
 338 **of LER on the blades. Afterwards, high-resolution SfM could be applied to quantify the severity of**
 339 **the located erosion, which could be used to estimate the aerodynamic impact. Furthermore, if these**
 340 **inspections were combined with a probabilistic model such as a dynamic Bayesian network model**
 341 **[69], the development of the erosion in time could be estimated. This would provide an input for when**
 342 **to conduct repairs on the blade.**

343 5. Conclusion

344 **This proof-of-principle study demonstrated the successful application of high-resolution SfM to**
 345 **quantify the surface roughness of a decommissioned turbine blade. To better resemble the LE erosion**
 346 **observed from inspections, a severe level of erosion with a large area of delamination was applied to the**
 347 **blade. To mimic realistic inspection conditions, the blade was hanged vertically in an outdoor setting,**

348 and the SfM image acquisition was conducted hand-held to ensure a level of vibrations. Using a 300
349 mm focal length and 2 m distance from the blade, a 1 mm spatial resolution of the SfM reconstruction
350 was obtained.

351 To validate the SfM scan, smaller regions of interest were transferred to the lab using replication
352 moulding and measured with confocal microscopy. From the co-registered SfM and reference regions, a
353 number of surface roughness parameters and topographic feature size were extracted. The quantitative
354 results of surface roughness and topographic feature sizes displayed sub-mm accuracies. Compared to
355 the reference, the RMSD value was $9\ \mu\text{m}$ for the S_q roughness using an S-filter of 0.025 mm and L-filter
356 of 10 mm, while the RMSD value was 0.1 mm for the depths and heights of topographic features. The
357 results demonstrate the potential for using high-resolution SfM for quantitative measurement of LER
358 on wind turbine blades. Quantitative measurements of LER from blades in operation could aid in
359 creating more realistic CFD models and improve blade inspections.

360 In future work, a high-resolution SfM inspection using a UAV should be carried out on the blade
361 of a wind turbine in operation. The camera would be mounted in a gantry on the UAV platform to
362 allow for the same poses relative to the blade as in the current study. These settings would allow a
363 more thorough investigation of the effects of vibrations from UAV platform and turbine on the image
364 acquisition and the quality of the 3D reconstructions. In addition, the sensitivity of high-resolution SfM
365 towards surface roughness should be investigated further through measurements on blade surfaces
366 of varying erosion severity. Further studies are also needed on the influence of the texture and color
367 contrast of the blade surface on the quality of the reconstructed surface details.

368 **Author Contributions:** The research was conceptualized by CBM and JG. MSN, EKK and IN developed the
369 methodology and performed the data collection. Visualization was performed by MSN and IN. MSN performed
370 data analysis and validation and wrote the original draft with input from IN and EKK. CBM and JG supervised
371 the research activity and made suggestions for revision. All authors have read and agreed to the published version
372 of the manuscript.

373 **Funding:** This work has received funding by the Energy Technology Development and Demonstration Program
374 (project number 64015-0046) under the Danish Energy Agency. MSN and JG were also supported by funds from
375 the Danish Agency for Institutions and Educational Grants.

376 **Conflicts of Interest:** The authors declare no conflict of interest. The funders had no role in the design of the
377 study; in the collection, analyses, or interpretation of data; in the writing of the manuscript, or in the decision to
378 publish the results.

379 Abbreviations

380 The following abbreviations are used in this manuscript:

381 LE	Leading Edge
LER	Leading Edge Roughness
SfM	Structure-from-Motion
UAV	Unmanned Aerial Vehicle
CM	Confocal Microscopy
382 DEM	Digital Elevation Model
GSD	Ground Sampling Distance
ITF	Instrument Transfer Function
CCF	Cross-Correlation Function
RMSD	Root Mean Square Deviation

383

- 384 1. Zidane, I.F.; Saqr, K.M.; Swadener, G.; Ma, X.; Shehadeh, M.F. On the role of surface roughness in the
385 aerodynamic performance and energy conversion of horizontal wind turbine blades: a review. *International*
386 *Journal of Energy Research* **2016**, *40*, 2054–2077. doi:10.1002/er.3580.

- 387 2. White, E.; Kutz, D.; Freels, J.; Monschke, J.; Grife, R.; Sun, Y.; Chao, D. Leading-Edge Roughness Effects
388 on 63(3)-418 Airfoil Performance. 49th AIAA Aerospace Sciences. American Institute of Aeronautics and
389 Astronautics (AIAA), 2011. doi:10.2514/6.2011-352.
- 390 3. Yang, K. Geometry Design Optimization of a Wind Turbine Blade Considering Effects on Aerodynamic
391 Performance by Linearization. *Energies* **2020**, *13*, 2320.
- 392 4. Sareen, A.; Sapre, C.A.; Selig, M.S. Effects of leading edge erosion on wind turbine blade performance.
393 *Wind Energy* **2014**, *17*, 1531–1542. doi:10.1002/we.1649.
- 394 5. Langel, C.M.; Chow, R.; Hurley, O.F.; Van Dam, C.C.P.; Maniaci, D.C.; Ehrmann, R.S.; White, E.B.
395 Analysis of the Impact of Leading Edge Surface Degradation on Wind Turbine Performance. 33rd
396 Wind Energy Symposium; American Institute of Aeronautics and Astronautics: Reston, Virginia, 2015.
397 doi:10.2514/6.2015-0489.
- 398 6. Han, W.; Kim, J.; Kim, B. Effects of contamination and erosion at the leading edge of blade tip
399 airfoils on the annual energy production of wind turbines. *Renewable Energy* **2018**, *115*, 817–823.
400 doi:10.1016/j.renene.2017.09.002.
- 401 7. Darbandi, M.; Mohajer, A.; Behrouzifar, A.; Jalali, R.; Schneider, G.E. Evaluating the effect of blade surface
402 roughness in megawatt wind turbine performance using analytical and numerical approaches. 10th
403 International Conference on Heat Transfer, Fluid Mechanics and Thermodynamics, 2014, number July, pp.
404 800–805.
- 405 8. Schramm, M.; Rahimi, H.; Stoevesandt, B.; Tangager, K. The Influence of Eroded Blades on Wind Turbine
406 Performance Using Numerical Simulations. *Energies* **2017**, *10*, 1420. doi:10.3390/en10091420.
- 407 9. Gaudern, N. A practical study of the aerodynamic impact of wind turbine blade leading edge erosion.
408 *Journal of Physics: Conference Series* **2014**, *524*, 012031. doi:10.1088/1742-6596/524/1/012031.
- 409 10. Tchakoua, P.; Wamkeue, R.; Ouhrouche, M.; Slaoui-Hasnaoui, F.; Tameghe, T.; Ekemb, G. Wind Turbine
410 Condition Monitoring: State-of-the-Art Review, New Trends, and Future Challenges. *Energies* **2014**,
411 *7*, 2595–2630. doi:10.3390/en7042595.
- 412 11. Wang, L.; Zhang, Z. Automatic Detection of Wind Turbine Blade Surface Cracks Based on UAV-Taken
413 Images. *IEEE Transactions on Industrial Electronics* **2017**, *64*, 7293–7303. doi:10.1109/TIE.2017.2682037.
- 414 12. Peng, L.; Liu, J. Detection and analysis of large-scale WT blade surface cracks based on UAV-taken images.
415 *IET Image Processing* **2018**, *12*, 2059–2064. doi:10.1049/iet-ipr.2018.5542.
- 416 13. Shihavuddin, A.; Chen, X.; Fedorov, V.; Nymark Christensen, A.; Andre Brogaard Riis, N.; Branner, K.;
417 Bjorholm Dahl, A.; Reinhold Paulsen, R. Wind Turbine Surface Damage Detection by Deep Learning Aided
418 Drone Inspection Analysis. *Energies* **2019**, *12*, 676. doi:10.3390/en12040676.
- 419 14. Durdevic, P.; Ortiz-Arroyo, D.; Yang, Z. LiDAR Assisted Camera Inspection of Wind Turbines:
420 Experimental Study. 2019 1st International Conference on Electrical, Control and Instrumentation
421 Engineering (ICECIE). IEEE, 2019, pp. 1–7.
- 422 15. Wang, Y.; Yoshihashi, R.; Kawakami, R.; You, S.; Harano, T.; Ito, M.; Komagome, K.; Iida, M.; Naemura, T.
423 Unsupervised anomaly detection with compact deep features for wind turbine blade images taken by a
424 drone. *IPSN Transactions on Computer Vision and Applications* **2019**, *11*, 1–7.
- 425 16. Zhang, D.; Watson, R.; Dobie, G.; MacLeod, C.; Khan, A.; Pierce, G. Quantifying impacts on remote
426 photogrammetric inspection using unmanned aerial vehicles. *Engineering Structures* **2020**, p. 109940.
- 427 17. Sturzenegger, M.; Stead, D. Close-range terrestrial digital photogrammetry and terrestrial laser scanning
428 for discontinuity characterization on rock cuts. *Engineering Geology* **2009**, *106*, 163–182.
- 429 18. Westoby, M.; Brasington, J.; Glasser, N.; Hambrey, M.; Reynolds, J.
430 ‘Structure-from-Motion’ photogrammetry: A low-cost, effective tool for geoscience applications.
431 *Geomorphology* **2012**, *179*, 300–314.
- 432 19. Favalli, M.; Fornaciai, A.; Isola, I.; Tarquini, S.; Nannipieri, L. Multiview 3D reconstruction in geosciences.
433 *Computers & Geosciences* **2012**, *44*, 168–176. doi:https://doi.org/10.1016/j.cageo.2011.09.012.
- 434 20. VisualSFM, C.W. A visual structure from motion system, 2011.
- 435 21. Sweeney, C.; Hollerer, T.; Turk, M. Theia: A fast and scalable structure-from-motion library. Proceedings of
436 the 23rd ACM international conference on Multimedia. ACM, 2015, pp. 693–696.
- 437 22. Agisoft. Metashape. <http://www.agisoft.com/>, 2010. Accessed: 2019-09-20.
- 438 23. Bentley: ContextCapture. <https://www.bentley.com/en/products/brands/contextcapture>. Accessed:
439 2019-03-06.

- 440 24. CapturingReality. CapturingReality: Reality Capture. <https://www.capturingreality.com/>, 2016.
441 Accessed: 2020-05-06.
- 442 25. Siebert, S.; Teizer, J. Mobile 3D mapping for surveying earthwork projects using an Unmanned Aerial
443 Vehicle (UAV) system. *Automation in Construction* **2014**, *41*, 1–14.
- 444 26. Han, K.K.; Golparvar-Fard, M. Appearance-based material classification for monitoring of operation-level
445 construction progress using 4D BIM and site photologs. *Automation in Construction* **2015**, *53*, 44–57.
446 doi:10.1016/J.AUTCON.2015.02.007.
- 447 27. Tuttas, S.; Braun, A.; Borrmann, A.; Stilla, U. Acquisition and Consecutive Registration of Photogrammetric
448 Point Clouds for Construction Progress Monitoring Using a 4D BIM. *PFG—Journal of Photogrammetry, Remote
449 Sensing and Geoinformation Science* **2017**, *85*, 3–15.
- 450 28. Jahanshahi, M.R.; Masri, S.F.; Padgett, C.W.; Sukhatme, G.S. An innovative methodology for detection and
451 quantification of cracks through incorporation of depth perception. *Machine vision and applications* **2013**, pp.
452 1–15.
- 453 29. Chaayasarn, K.; Kim, T.K.; Viola, F.; Cipolla, R.; Soga, K. Distortion-Free Image Mosaicing for Tunnel
454 Inspection Based on Robust Cylindrical Surface Estimation through Structure from Motion. *Journal of
455 Computing in Civil Engineering* **2016**, *30*, 4015045. doi:10.1061/(ASCE)CP.1943-5487.0000516.
- 456 30. Stent, S.; Gherardi, R.; Stenger, B.; Soga, K.; Cipolla, R. Visual change detection on tunnel linings. *Machine
457 Vision and Applications* **2016**, *27*, 319–330.
- 458 31. Masson, J.E.N.; Petry, M.R. Comparison of mesh generation algorithms for railroad reconstruction.
459 Autonomous Robot Systems and Competitions (ICARSC), 2017 IEEE International Conference on. IEEE,
460 2017, pp. 266–271.
- 461 32. Khaloo, A.; Lattanzi, D. Hierarchical Dense Structure-from-Motion Reconstructions for Infrastructure
462 Condition Assessment. *Journal of Computing in Civil Engineering* **2017**, *31*, 04016047.
463 doi:10.1061/(ASCE)CP.1943-5487.0000616.
- 464 33. Schöning, J.; Heidemann, G. Evaluation of multi-view 3D reconstruction software. International Conference
465 on Computer Analysis of Images and Patterns. Springer, 2015, pp. 450–461.
- 466 34. Nikolov, I.; Madsen, C. Benchmarking Close-range Structure from Motion 3D Reconstruction Software
467 Under Varying Capturing Conditions. Euro-Mediterranean Conference. Springer, 2016, pp. 15–26.
- 468 35. Lowe, D.G. Distinctive image features from scale-invariant keypoints. *International journal of computer
469 vision* **2004**, *60*, 91–110.
- 470 36. Rublee, E.; Rabaud, V.; Konolige, K.; Bradski, G. ORB: An efficient alternative to SIFT or SURF. 2011
471 International conference on computer vision. Ieee, 2011, pp. 2564–2571.
- 472 37. Wu, C. Towards linear-time incremental structure from motion. 3DTV-Conference, 2013 International
473 Conference on. IEEE, 2013, pp. 127–134.
- 474 38. Smith, M.W.; Carrivick, J.L.; Quincey, D.J. Structure from motion photogrammetry in physical geography.
475 *Progress in Physical Geography: Earth and Environment* **2016**, *40*, 247–275. doi:10.1177/0309133315615805.
- 476 39. D’Amico, N.; Yu, T. Accuracy analysis of point cloud modeling for evaluating concrete specimens. SPIE
477 Smart Structures and Materials+ Nondestructive Evaluation and Health Monitoring. International Society
478 for Optics and Photonics, 2017, pp. 101691D–101691D.
- 479 40. Micheletti, N.; Chandler, J.H.; Lane, S.N. Investigating the geomorphological potential of freely available
480 and accessible structure-from-motion photogrammetry using a smartphone. *Earth Surface Processes and
481 Landforms* **2015**, *40*, 473–486. doi:10.1002/esp.3648.
- 482 41. Smith, M.W.; Vericat, D. From experimental plots to experimental landscapes: topography, erosion and
483 deposition in sub-humid badlands from Structure-from-Motion photogrammetry. *Earth Surface Processes
484 and Landforms* **2015**, *40*, 1656–1671. doi:10.1002/esp.3747.
- 485 42. Micheletti, N.; Chandler, J.H.; Lane, S.N. Structure from Motion (SfM) Photogrammetry. In *Geomorphological
486 Techniques*, Online Ed. ed.; British Society for Geomorphology Geomorphological Techniques, 2015; chapter
487 2.2, pp. 1–12.
- 488 43. Harwin, S.; Lucieer, A. Assessing the Accuracy of Georeferenced Point Clouds Produced via Multi-View
489 Stereopsis from Unmanned Aerial Vehicle (UAV) Imagery. *Remote Sensing* **2012**, *4*, 1573–1599.
490 doi:10.3390/rs4061573.
- 491 44. Kersten, T.P.; Lindstaedt, M. Image-based low-cost systems for automatic 3D recording and modelling of
492 archaeological finds and objects. Euro-Mediterranean Conference. Springer, 2012, pp. 1–10.

- 493 45. Thoeni, K.; Giacomini, A.; Murtagh, R.; Kniest, E. A comparison of multi-view 3D reconstruction of a rock
494 wall using several cameras and a Laser scanner. *International Archives of the Photogrammetry, Remote Sensing*
495 *and Spatial Information Sciences - ISPRS Archives* **2014**, *40*, 573–580. doi:10.5194/isprsarchives-XL-5-573-2014.
- 496 46. James, M.R.; Robson, S. Straightforward reconstruction of 3D surfaces and topography with a
497 camera: Accuracy and geoscience application. *Journal of Geophysical Research: Earth Surface* **2012**, *117*.
498 doi:10.1029/2011JF002289.
- 499 47. Goetz, J.; Brenning, A.; Marcer, M.; Bodin, X. Modeling the precision of structure-from-motion multi-view
500 stereo digital elevation models from repeated close-range aerial surveys. *Remote Sensing of Environment*
501 **2018**, *210*, 208–216. doi:10.1016/J.RSE.2018.03.013.
- 502 48. Tavani, S.; Corradetti, A.; Billi, A. High precision analysis of an embryonic extensional fault-related fold
503 using 3D orthorectified virtual outcrops: The viewpoint importance in structural geology. *Journal of*
504 *Structural Geology* **2016**, *86*, 200–210. doi:10.1016/J.JSG.2016.03.009.
- 505 49. Corradetti, A.; McCaffrey, K.; De Paola, N.; Tavani, S. Evaluating roughness scaling properties of
506 natural active fault surfaces by means of multi-view photogrammetry. *Tectonophysics* **2017**, *717*, 599–606.
507 doi:10.1016/j.tecto.2017.08.023.
- 508 50. Hansen, H.; Hocken, R.; Tosello, G. Replication of micro and nano surface geometries. *CIRP Annals -*
509 *Manufacturing Technology* **2011**, *60*, 695–714. doi:10.1016/j.cirp.2011.05.008.
- 510 51. Nilsson, L.; Ohlsson, R. Accuracy of replica materials when measuring engineering surfaces. *International*
511 *Journal of Machine Tools and Manufacture* **2001**, *41*, 2139–2145. doi:10.1016/S0890-6955(01)00080-3.
- 512 52. Gasparin, S.; Hansen, H.N.; Tosello, G. Traceable surface characterization using replica moulding
513 technology, 2011.
- 514 53. Liu, Y.C.; Ling, C.Y.; Malcolm, a.a.; Dong, Z.G. Accuracy of replication for non-destructive surface finish
515 measurement. Singapore International NDT Conference & Exhibition, 2011, pp. 3–4.
- 516 54. Walton, K.; Fleming, L.; Goodhand, M.; Racasan, R.; Zeng, W. High fidelity replication of surface texture
517 and geometric form of a high aspect ratio aerodynamic test component. *Surface Topography: Metrology and*
518 *Properties* **2016**, *4*, 025003. doi:10.1088/2051-672X/4/2/025003.
- 519 55. Baruffi, F.; Parenti, P.; Cacciatore, F.; Annoni, M.; Tosello, G. On the Application of Replica Molding
520 Technology for the Indirect Measurement of Surface and Geometry of Micromilled Components.
521 *Micromachines* **2017**, *8*, 195. doi:10.3390/mi8060195.
- 522 56. Kumar, C.; Palacios, A.; Surapaneni, V.A.; Bold, G.; Thielen, M.; Licht, E.; Higham, T.E.; Speck, T.; Le
523 Hou erou, V. Replicating the complexity of natural surfaces: Technique validation and applications for
524 biomimetics, ecology and evolution. *Philosophical Transactions of the Royal Society A: Mathematical, Physical*
525 *and Engineering Sciences* **2019**, *377*. doi:10.1098/rsta.2018.0265.
- 526 57. Bak, C.; Gaunaa, M.; Olsen, A.S.; Kruse, E.K. What is the critical height of leading edge roughness for
527 aerodynamics. *Journal of Physics: Conference Series*, 2016, Vol. 753, p. 022023.
- 528 58. Sch oning, J.; Heidemann, G. Taxonomy of 3D Sensors-A Survey of State-of-the-Art Consumer
529 3D-Reconstruction Sensors and their Field of Applications. VISIGRAPP (3: VISAPP), 2016, pp. 194–199.
- 530 59. Nikolov, I.; Madsen, C. Performance Characterization of Absolute Scale Computation for 3D Structure from
531 Motion Reconstruction. 14th International Joint Conference on Computer Vision, Imaging and Computer
532 Graphics Theory and Applications (Visigrapp 2019) International Conference on Computer Vision Theory
533 and Applications. SCITEPRESS Digital Library, 2019, pp. 884–891.
- 534 60. Girardeau-Montaut, D. CloudCompare. <http://www.cloudcompare.org/>. Accessed: 2019-03-06.
- 535 61. Struers 2010 RepliSet Technical Data Sheet. [https://www.struers.com/en/Products/Materialographic-](https://www.struers.com/en/Products/Materialographic-analysis/Materialographic-analysis-equipment/Replication-system)
536 [analysis/Materialographic-analysis-equipment/Replication-system](https://www.struers.com/en/Products/Materialographic-analysis/Materialographic-analysis-equipment/Replication-system). Accessed: 2020-03-06.
- 537 62. Jolivet, S.; Mezghani, S.; El Mansori, M. Multiscale analysis of replication technique efficiency for 3D
538 roughness characterization of manufactured surfaces. *Surface Topography: Metrology and Properties* **2016**,
539 *4*, 035002. doi:10.1088/2051-672X/4/3/035002.
- 540 63. PLU NEOX confocal microscope. [https://www.sensofar.com/sensofar-introduces-their-most-advanced-](https://www.sensofar.com/sensofar-introduces-their-most-advanced-optical-3d-profiler-plu-neox/#)
541 [optical-3d-profiler-plu-neox/#](https://www.sensofar.com/sensofar-introduces-their-most-advanced-optical-3d-profiler-plu-neox/#). Accessed: 2020-03-06.
- 542 64. Scanning Probe Image Processor (SPIP). <https://www.imagemet.com/products/spip/>. Accessed:
543 2020-03-06.
- 544 65. de Groot, P.; de Lega, X.C. Interpreting interferometric height measurements using the instrument transfer
545 function. In *Fringe 2005*; Springer Berlin Heidelberg, 2006; pp. 30–37. doi:10.1007/3-540-29303-5_3.

- 546 66. Song, J.; Vorburger, T.; Ma, L.; Libert, J.; Ballou, S. A metric for the comparison of surface topographies of
547 standard reference material (SRM) bullets and casings. Proceedings of the 20th Annual ASPE Meeting,
548 ASPE 2005, 2005.
- 549 67. ISO 25178-3(2012) Geometrical product specifications (GPS) – Surface texture: Areal – Part 3: Specification
550 operators. <https://www.iso.org/standard/42895.html>. Accessed: 2020-03-05.
- 551 68. ISO 25178 Geometrical product specifications (GPS) – Surface texture: Areal – Part 2: Terms, definitions
552 and surface texture parameters. <https://www.iso.org/standard/42785.html>. Accessed: 2020-03-05.
- 553 69. Nielsen, J.S.; Sørensen, J.D. Bayesian estimation of remaining useful life for wind turbine blades. *Energies*
554 **2017**, *10*, 664.

555 © 2020 by the authors. Submitted to *Energies* for possible open access publication under the terms and conditions
556 of the Creative Commons Attribution (CC BY) license (<http://creativecommons.org/licenses/by/4.0/>).